Amplifying oxidative stress utilizing multiband luminescence of lanthanide nanoparticles for eliciting systemic antitumor immunity

Fengxia Wu [a,b], Haoran Chen [a], Qiqing Li [a], Ruiqi Liu [b], Yongkuan Suo [b], Bin Li [a], Xianggui Kong [a], Zhen Cheng [c,d], Hongguang Liu [b,*], Yulei Chang [a,*]

[a] State Key Laboratory of Luminescence and Applications, Changchun Institute of Optics, Fine Mechanics and Physics, Chinese Academy of Sciences, Changchun 130033, Jilin, China
[b] Institute of Molecular Medicine, College of Life and Health Sciences, Northeastern University, Shenyang 110169, Liaoning, China
[c] State Key Laboratory of Drug Research, Molecular Imaging Center, Shanghai Institute of Materia Medica, Chinese Academy of Sciences, Shanghai 201203, China
[d] Shandong Laboratory of Yantai Drug Discovery, Bohai Rim Advanced Research Institute for Drug Discovery, Yantai 264117, Shandong, China

ARTICLE INFO

ABSTRACT

Reactive oxygen species (ROS) are closely related to innate and adaptive immune responses in tumor immunotherapy. ROS-mediated therapies show great hope in improving therapeutic efficacy by inducing immunogenic cell death. However, the efficiency is still limited by the poor ROS production rate. Herein, a ROS nanogenerator is designed to boost antitumor immunity, integrating with pH-dissociable Fe^{3+}-gallic acid (Fe-GA) complex as the shell and photosensitizer (Chlorin e6, Ce6)-coupled lanthanide-doped luminescence nanoparticles (LnNPs) as the core. Upon near-infrared (NIR) light irradiation, LnNPs exhibit multiband upconversion emission from ultraviolet (UV) to visible (Vis) and downshifting emission in the promising second NIR imaging region (NIR-II, 1550 nm). Especially, the UV photons and reducing agent GA could respectively mediate the reduction of Fe^{3+}, allowing more Fe^{2+} to participate in the Fenton reaction to generate hydroxyl radicals (•OH) for ferroptosis therapy (FT). Besides, the UV–Vis upconversion emission can activate the coupling photosensitizer-Ce6 to generate $^1O_2$ for photodynamic therapy (PDT). Additionally, Fe-GA can serve as a photothermal therapy (PTT) agent; in turn, hyperthermia enhances ROS generation. Our rational-designed Ln@Fe NPs could not only enhance the synergistic antitumor efficiency by boosting ROS generation but also effectively inhibit tumor metastasis by activating strong antitumor immunity, providing a paradigm for imaging-guided cancer treatment.

1. Introduction

Immunotherapy provides a new opportunity to prevent tumor recurrence and metastasis by boosting the innate immune system [1]. Currently, immune checkpoint blockers [2], chimeric antigen receptor-modified T cells (CAR-T)[3], and tumor vaccines [4] have shown promising results in cancer immunotherapy. Even so, due to insufficient immune system activation, immune checkpoint blockade therapy is only effective for a small proportion of patients [5]. CAR-T therapy has been reported to induce severe systemic side effects [6]. Additionally, it is challenging to design a common commercial vaccine due to the differences in neoantigens between patients [7]. Fortunately, inducing the immunogenic cell death (ICD) is a promising way to stimulate antitumor immune response with the release of danger-associated molecular patterns (DAMPs), including surface-exposed calreticulin (CRT), adenosine

triphosphate (ATP), and high-mobility group protein B1 (HMGB1) from dying cancer cells [8,9]. It is known that reactive oxygen species (ROS)-related treatments such as photodynamic therapy (PDT) [10–12] and ferroptosis therapy (FT) [13] can induce ICD. PDT is a minimally invasive and effective modality to ablate tumors with light irradiation. Although PDT has rapidly advanced due to its good spatiotemporal controllability and minimally invasive nature, its therapeutic efficacy is still unsatisfactory [14]. For example, the limited tissue penetration depth of the excitation light (i.e., visible) [15,16] and the complex tumor microenvironment (TME), i.e., hypoxic condition [17], attenuate the efficacy of O_2-dependent traditional PDT [18].

FT, another ROS-related therapy modality, induces cancer cell death via lipid peroxidation (LPO) accumulation [19,20]. Typically, ROS is generated based on the Fenton reaction, which converts H_2O_2 into hydroxyl radical (•OH) with the catalysis of iron ions (Fe^{2+} and Fe^{3+}).

Additionally, the potential mechanism of ferroptosis does not depend on external energy and oxygen, which circumvents the limitation of traditional PDT. However, the efficiency of the Fenton reaction is hindered by limited intracellular iron ion content and overexpressed antioxidants (e. g. GSH). Therefore, amplifying the intracellular oxidative stress and breaking the redox homeostasis is necessary to improve ROS-related treatment.

Recently, lanthanide-doped luminescence nanoparticles (LnNPs) were shown to possess potential in biomedicine, such as luminescence imaging [21], phototherapy [22], and biosensing [23], owing to their ability to convert near-infrared (NIR) light into multiband upconversion emissions from UV to the first NIR region (NIR-I), or downshift emission in the second NIR region (NIR-II) [24]. Together with high photochemical stability and large anti-/Stokes shift, LnNPs enable deep tissue penetration while reducing background luminescence, thus improving the signal-to-noise ratio (SNR) and clarity in tumor imaging [21]. Moreover, LnNPs are also used as energy converters to activate the coupled PSs to achieve deep-tissue PDT through Förster resonance energy transfer (FRET) [25,26]. The resulting NIR-nanophotosensitizer (NanoPS) is a promising theranostic nanoplatform that can improve the poor efficacy of PDT caused by limited tissue penetration and increase treatment accuracy under imaging guidance. To date, most LnNPs-based visualization PDT strategies were mainly guided by their upconversion luminescence (UCL), which suffers from drawbacks such as limited light penetration and imaging clarity. NIR-II imaging-guided PDT may offer a promising strategy for deep-seated tumors treatment. Thus, to attain satisfactory therapeutic effects, rationally designing a programmable theranostic nanoplatform by integrating multiple therapeutic strategies is highly desirable [27–29].

Herein, a TME-responsive ROS nanogenerator integrating LnNPs-Ce6 nanoPSs with Fe^{3+}-gallic acid (GA) complex was developed by boosting ROS generation to augment antitumor immune response (Scheme 1). In this nanoplatform, the multiband emissions of photo-switchable LnNPs were composed of multi-wavelength-excited NaErF$_4$:2%Ce core (808, 980, or 1530 nm) and a single-wavelength-excited NaYbF$_4$:0.5 %Tm emitting layer (980 nm). Notably, 2% Ce doping quenched the bright red upconversion emission of Er^{3+} to inhibit the FRET process (multiple excitations), enabling damage-free and real-time NIR-IIb imaging under 808 nm or 1530 nm excitation [30,31]. The Fe-GA complex can dissociate in mild acidic TME (pH 6.5 ~ 6.8), accompanied by the release of Fe^{3+} and GA. Notably, the UV upconversion emission could photo-reduce Fe^{3+} to Fe^{2+}; and GA, as a highly active reducing agent, could also convert Fe^{3+} into Fe^{2+}, enabling the Fe^{2+} to participate in the Fenton reaction to generate •OH [32]. The resulting •OH can promote the formation of LPO, which is essential for FT. Besides, Fe-GA can serve as a photothermal converter, which performs photothermal therapy (PTT). Upon NIR-II photoirradiation, the heat generated by Fe-GA enriched in the tumor can not only directly ablate tumors but also enhance the generation of ROS. The PTT/PDT/FT synergistic treatment induces a potent ICD effect, producing immune-related cytokines and inhibiting lung metastasis. Moreover, the Ln@Fe NPs possess NIR-IIb luminescence ($L_{1550\ Em,\ 808\ Ex}$) and photoacoustic (PA) imaging performance, realizing imaging-guided antitumor therapy.

2. Experimental section

2.1. Materials

RECl$_3$·6H$_2$O (RE = Er, Ce, 99.99%), Tm(CF$_3$COO)$_3$ (>99.9%), Yb (CF$_3$COO)$_3$ (>99.9%), oleic acid (OA, 90%), 1-octadecene (ODE, 90%), and poly (allylamine hydrochloride) (PAH·HCl, Mw ~ 15,000) were purchased from Sigma-Aldrich. NH$_4$F, NaOH, polyethene glycol-succinimidyl carbonate (PEG-SC), FeCl$_3$·6H$_2$O (99%), gallic acid (99%), and 1,10-phenanthroline (99%) were obtained from Aladdin (Shanghai, China). Hydrochloric acid (HCl), methanol, acetone, ethanol, and cyclohexane were obtained from Beijing Chemical Plant Co., Ltd. GSH assay kit, CCK-8 kit, Annexin V-FITC/PI were purchased from
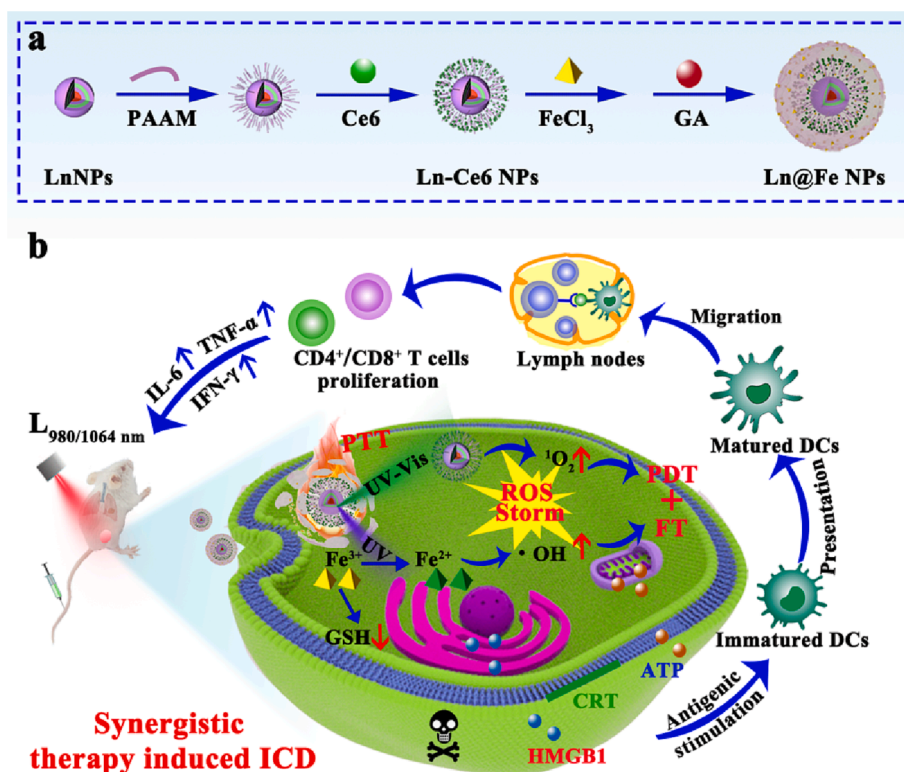
Scheme 1. Schematic illustration of the synthesis procedure and underlying antitumor mechanism of the Ln@Fe NPs. (a) The synthesis route of Ln@Fe NPs. (b) The proposed mechanism of Ln@Fe NPs for synergistic therapy-elicited immunotherapy.

Beijing Solarbio Science & Technology Co., Ltd. 2′, 7′-Dichlorofluorescein diacetate (DCFH-DA), GPX4 rabbit polyclonal antibody, β-actin mouse monoclonal antibody, AP-labeled goat anti-rabbit IgG, and BCIP/NBT Alkaline Phosphatase Color Development Kit were purchased from Beyotime Institute of Biotechnology (Nantong, China). Liperfluo and FerroOrange probe was purchased from Dojindo. All the chemicals were used without further purification.

2.2. Synthesis of LnNPs

Typically, 0.98 mmol $ErCl_3$ and 0.02 mmol $CeCl_3$ were added into a 100 mL three neck-flask containing 9 mL OA and 22.5 mL ODE. The mixture was degassed with argon and heated to 160 °C by stirring continuously to form a homogeneous solution. After the solution was cooled down to 60 °C, 4 mL methanol solution containing NaOH (100 mg) and NH_4F (148 mg) was added and stirred at 80 °C for 1 h to evaporate the methanol. Subsequently, the system was heated to 300 °C and stirred for 1.5 h under Argon protection. Afterwards, the $NaErF_4$:2% Ce core was collected by centrifugation, and the precipitate was dispersed into 8 mL cyclohexane.

The shell coating procedure is similar except for the precursor shell material of $Ln(CF_3COO)_3$ and the calculated total amount. 6 mL OA and 15 mL ODE were poured into a three neck-flask containing 1 mmol Y $(CF_3COO)_3$ and 1 mmol $NaCF_3COO$, and heated the mixture to 120 °C to form the shell precursor solution. After that, the solution was cooled to room temperature (RT), and as-prepared $NaErF_4$:2%Ce in cyclohexane solution was added. Then, the solution was heated to 85 °C to remove cyclohexane. Subsequently, the mixture was heated to 300 °C and kept for 1.5 h under Argon protection. After centrifugation, the as-prepared LnNPs were obtained.

2.3. Synthesis of LnNPs-Ce6

Ligand-free LnNPs were obtained by the acid-treated method. Briefly, 2 mL of hydrochloric acid (0.1 M) was added to 2 mL LnNPs in cyclohexane solution under stirring until LnNPs were transferred entirely to the aqueous phase. Next, ligand-free LnNPs were collected by centrifugation (12,000 rpm, 20 min) and redispersed in DMF. After that, 10 mg LnNPs were mixed with 100 μL PAAm (Poly allylamine solution, 20 wt%) aqueous solution and stirred overnight. After removing excess PAAm through centrifugation, the LnNPs-PAAm was incubated with 0.3 mg Ce6 (1 mg mL^{-1} in DMF) and an excess amount of EDC and NHS. The solution was stirred at RT for 24 h. Finally, LnNPs-Ce6 were collected by centrifugation and resuspended in deionized water for further use.

2.4. Synthesis of Ln@Fe NPs

Typically, 5 mg of LnNPs-Ce6 aqueous solution was incubated with 15 mg of PEG-SC for 6 h at RT. After that, 10 mg of $FeCl_3 \cdot 6H_2O$ was added and stirred for 60 min at RT. Then, 5 mg of gallic acid (GA) was added to the above solution and stirred overnight at RT. Finally, LnNPs-Ce6@Fe (named Ln@Fe NPs) were collected by centrifugation (12,000 rpm, 20 min) and redispersed in deionized water for further use.

2.5. Photothermal property of Ln@Fe NPs

To evaluate the photothermal performance of Ln@Fe NPs with various Fe/GA ratios, 1 mL of NPs aqueous solutions (4.5 mg mL^{-1}) were irradiated by a 1064 nm laser (1 W cm^{-2}, 10 min). The temperature change was recorded using a thermal imaging system (FLIR) every 30 s.

2.6. Release kinetics of Fe^{3+}

To investigate the release kinetics of Fe^{3+}, the Ln@Fe NPs were dispersed in different pH buffers and stirred at RT. Then, the released Fe^{3+} in the supernatants at different times (0.5, 1, 1.5, 2, 4, 8, and 12 h)

was collected by centrifugation, and the UCL spectra were recorded under 980 nm excitation.

2.7. Singlet oxygen detection ($^1O_2$)

DPBF was chosen to monitor the $^1O_2$. Briefly, 10 μL of DPBF solution (5 mM) in DMF was added to the 1 mL sample suspension (LnNPs-Ce6 or different pH buffer treated Ln@Fe NPs), respectively. Then, the mixture was irradiated by a 980 nm laser (0.7 W cm^{-2}) for 20 min, and the absorption spectra of DPBF were recorded every 5 min.

2.8. Detect the conversion of Fe^{3+} to Fe^{2+}

To determine the conversion of Fe^{3+} to Fe^{2+} induced by UV and GA, Ln@Fe NPs were dispersed in buffers with different pH and irradiated with NIR laser (980 nm). The Fe^{2+} can react with 1,10-phenanthroline (5 mM) to form a new complex, and with a maximum absorbance at 510 nm. The absorbance of the complex was monitored using UV–visible spectrophotometer.

2.9. Generation of •OH

The •OH generation was evaluated by MB degradation. Briefly, Ln@Fe NPs suspension (5 mg mL^{-1}, 50 μL) was added in different pH buffers containing H_2O_2 (10 mM) and MB (10 μg mL^{-1}) and with or without GSH (10 mM). Finally, the reaction system was centrifuged and measured the absorbance spectra of the supernatant.

2.10. Cell culture

Murine breast carcinoma cell line 4 T1 cells and mouse fibroblast cells (L929) were obtained from the Institute of Basic Medicine, Chinese Academy of Medical Science. 4 T1 cells were cultured in RPMI-1640 medium containing 10% fetal bovine serum (FBS) and 1% penicillin/streptomycin at 37 °C under a 5% CO_2 atmosphere. Normal cells (L929) were cultured in dulbecco modified eagle medium (DMEM) containing 10% fetal bovine serum (FBS) and 1% penicillin/streptomycin.

2.11. In vitro cellular uptake

Briefly, 4 T1 cells were seeded in 20-mm dishes at a density of 1.0×10^5 cells/well. After adhering overnight, the cells were incubated with Ln@Fe NPs (100 μg mL^{-1}) for 6 h. After rinsing three times with PBS, 4 T1 cells were fixed with paraformaldehyde (4%) for 15 min at 37 °C and washed three times. Finally, 4 T1 cells were captured by confocal laser scanning microscope (CLSM, Nikon) after staining with DAPI solution (0.5 μg mL^{-1}) for 10 min at 37 °C. To further quantitatively evaluate the endocytosis of nanoparticles by 4 T1 cells, the intracellular Fe content was measured by inductively coupled plasma-mass spectrometry (ICP-MS) after incubated with Ln@Fe NPs for different times (0, 6, 12, and 24 h).

2.12. Detection of intracellular Fe^{2+}

The FerroOrange probe was used to detect intracellular Fe^{2+}. Briefly, 4 T1 cells were cultured in 20-mm dishes and incubated overnight. Then, the cells were washed three times after incubated with Ln@Fe NPs for different times (0, 6, and 24 h). The FerroOrange probe was added to each well and incubated for 30 min at 37 °C. Finally, the cells were washed and imaged with a fluorescence microscope.

2.13. Intracellular reactive oxygen species (ROS) generation

The ROS-sensitive probe DCFH-DA was used to detect intracellular ROS generation induced by Ln@Fe NPs. Briefly, 4 T1 cells were seeded in 20-mm dishes at a 1.0×10^5/well density and incubated overnight.

The cells were divided into four groups including (1) PBS, (2) Ln@Fe NPs (3) Ln@Fe NPs + deferoxamine (DFO, a ferroptosis inhibitor), and (4) Ln@Fe NPs + $L_{980 + 1064}$ (0.6 W cm^{-2}, 6 min). The cells were washed with 1640 (free of FBS) three times after different treatments for 6 h. After that, DCFH-DA (10 μM) in 1640 (free of FBS) was added to each well and incubated for 30 min at 37 °C. Finally, the cells were washed three times and imaged with a fluorescence microscope.

2.14. Intracellular GSH, GPX4, and LPO evaluation

4 T1 cells were treated with different formulations including PBS, Ln@Fe NPs (200 μg mL^{-1}), Ln@Fe NPs + DFO, and Ln@Fe NPs + $L_{980 + 1064 nm}$ (0.6 W cm^{-2}, 6 min). After incubation for 6 h, the treated cells were collected to determine intracellular GSH content using the GSH assay kit (Solarbio, Beijing). Then, the intracellular GPX4 expression level was measured. The 4 T1 cells were collected and lysed after different treatments. Next, the proteins were separated by SDS-PAGE for Western blotting assay. In addition, liperfluo as an LPO probe (Dojindo) was applied for intracellular LPO detection, and a CLMS imaging system collected the results.

2.15. Bio-TEM imaging

4 T1 cells were incubated with Ln@Fe NPs (200 μg mL^{-1}) for 12 h, and the cells were collected after being washed with PBS three times. After that, the cells were fixed with 2.5% glutaric dialdehyde solution for bio-TEM imaging.

2.16. In vitro cytotoxicity

CCK-8 assay was used to assess the cytotoxicity under different treatments. To explore the ferroptosis therapy efficiency *in vitro* induced by Ln@Fe NPs, blocking studies were carried out using DFO. Typically, 4 T1 cells (1 × 10^4) were seeded into a 96-wells cell culture plate and incubated overnight. Then the cells were incubated with different concentrations of Ln@Fe NPs (0, 12.5, 25, 50, 100, and 200 μg mL^{-1}) with or without DFO (100 μM) for 24 h. For phototherapy, after incubated with Ln@Fe NPs for 6 h, the cells were irradiated with 980 + 1064 nm

$$hemolysis(\%) = (sample\ absorbance - PBS\ absorbance)/(H_2O\ absorbance - PBS\ absorbance) \times 100$$

laser (0.6 W cm^{-2}, 6 min). Finally, a CCK-8 assay was applied to determine the relative cell viability. Furthermore, a live/dead cell staining assay was performed to visualize the synergistic therapeutic effect. Briefly, 4 T1 cells cultured in 20-mm plates at a density of 1 × 10^5 cells/well, and were treated with PBS, Ln@Fe NPs, Ln@Fe NPs + DFO, and Ln@Fe NPs + $L_{980 + 1064}$ (0.6 W cm^{-2}, 6 min) for 6 h. Finally, the cells were observed with a fluorescence microscope after being stained with calcein AM and PI probes for 30 min.

2.17. Lysosome damage study

For the lysosome damage study, 4 T1 cells were seeded in 20-mm dishes at a density of 1.0 × 10^5 and incubated overnight. Then, the cells were divided into four groups in the manner mentioned above. Next, after different treatments, the cells were incubated with Lyso-Tracker Red (50 nM) for 30 min at 37 °C. Finally, 4 T1 cells were visualized by CLSM after further wishing three times with PBS.

2.18. ICD biomarkers detection

The 4 T1 cells were treated with PBS, Ln@Fe NPs, and Ln@Fe NPs +

$L_{980 + 1064 nm}$, respectively. After incubation for 6 h, the exposure of CRT was evaluated by immunofluorescence staining and the secretion of HMGB1 in the supernatant was detected by enzyme-linked immunosorbent assay (ELISA). Intracellular ATP level was measured using the ATP assay kit (Beyotime Biotechnology).

2.19. In vitro dendritic cells stimulation

Bone marrow-derived dendritic cells (BMDCs) were obtained from BALB/c mice and cultured in an RPMI-1640 medium containing 10% FBS, GM-CSF (20 ng mL^{-1}), and IL-4 (10 ng mL^{-1}). For *in vitro* DCs stimulation, the 4 T1cells after different treats with PBS, Ln@Fe NPs, or Ln@Fe NPs + $L_{980 + 1064 nm}$ were seeded in the upper chamber of Transwell system, and DCs were seeded in lower chamber for co-incubating for another 24 h. Then, the DCs were collected and stained with anti-CD11c-APC, anti-CD80-FITC, and anti-CD86-PE for flow cytometry. What's more, the secretion of IL-6 and TNF-α was evaluated by ELISA assay.

2.20. Tumor model

Female BALB/c mice (6–8 weeks, weighted 18–22 g) were purchased from Vital River Company in Beijing, and all animal experiments were performed in accordance with guidelines reviewed by the Laboratory Animal Management Committee of Northeastern University. First, 100 μL 4 T1 cells (1.0 × 10^6) in PBS were subcutaneously injected into the right flank of each mouse. The formula calculated the tumors volumes: V = a × b^2/2 mm^3 (a: Length; b: Width). When the tumor volumes reached about 60 mm^3, the *in vivo* experiments were then conducted.

2.21. Hemolysis assay

Red blood cells (RBCs) were obtained from the whole blood, then washed with PBS at least 3 times. After that, the RBCs (2%) were mixed with Ln@Fe NPs with different concentrations (0 – 400 μg mL^{-1}), and deionized water was used as a positive control. The absorbance of supernatants were determined after incubation at 37 °C for 2 h, the hemolysis radio was calculated:

2.22. In vivo NIR-II/PA imaging

4 T1 tumor-bearing mice were anesthetized with 5% chloral hydrate and injected intravenously (i.v.) with Ln@Fe NPs (200 μL, 10 mg kg^{-1}). For the *in vivo* NIR-II imaging, the luminescence images were recorded by the Imaging System (GH-SCS00) with an 808 nm laser excitation at different time points after administration. For the *in vivo* PA imaging, the PA images were collected by a PA imaging system (MSOT invision 128, Germany).

2.23. In vivo synergistic treatments

The tumor-bearing mice were randomly divided into four groups (n = 4): saline (G1), saline + $L_{980 + 1064 nm}$ (0.6 W cm^{-2}, 10 min) (G2), Ln@Fe NPs (G3), and Ln@Fe NPs + $L_{980 + 1064 nm}$ (0.6 W cm^{-2}, 10 min) (G4). The temperature of tumor sites was recorded every minute using a thermal imaging system (FLIR) at 4 h laser irradiation. After the different treatments, the body weight and tumor volumes were recorded every other day. To further evaluate the therapeutic outcome, the mice were sacrificed and collected the tumors for histology analysis of H&E and TUNEL staining after the treatment for 14 days.

2.24. Immune responses and metastasis inhibition in vivo

The tumor-bearing mice were received saline or Ln@Fe NPs + L_{980} + $_{1064\ nm}$ (0.6 W cm^{-2}, 10 min) treatments, respectively. Serum samples were isolated for cytokine detection by ELISA according to the manufacturer's protocols on day 7. Then, the 4 T1 cells (2.0×10^5) were intravenously injected into mice. The mice were sacrificed on day 30, and the tumors and lungs were harvested and sectioned for immunofluorescence staining and H&E staining, respectively. Furthermore, H&E staining of crucial organs (heart, liver, spleen, lung, and kidney) were carried out to evaluate the biosafety of Ln@Fe NPs further.

2.25. Statistical analysis

All data are expressed as the mean ± standard deviation (SD), and the significance of differences among groups was evaluated with Student's *t*-test (*$p < 0.05$, **$p < 0.01$, ***$p < 0.001$).

3. Results and discussion

3.1. Synthesis and characterization of Ln@Fe NPs

The procedure for the synthesis of Ln@Fe NPs is presented in Scheme 1a. The LnNPs ($NaErF_4$:2%Ce@$NaYF_4$@$NaYbF_4$:0.5 %Tm@$NaYF_4$) and corresponding nanoPSs (LnNPs-Ce6) were prepared according to our previously reported method [33]. The powder X-ray diffraction (XRD) pattern confirmed a pure hexagonal phase of the LnNPs (Fig. S1) [33]. Then, the Fe-GA complex shell was coated on the surface of PEGylated LnNPs-Ce6 by coordination [34,35]. Transmission electron microscopy (TEM) image of Ln@Fe NPs showed a typical core-multishell structure with a uniform size of ~ 88.6 nm, in which the LnNPs were coated with an obscure outer layer (Fe-GA) (Fig. 1a). In addition, the hydrodynamic diameter of Ln@Fe NPs in the cell culture medium (1640 + 10% FBS) was monitored for 6 days. As demonstrated in Fig. S2, the average hydrodynamic diameter of Ln@Fe NPs changed slightly, and the polydispersity index (PDI) value was still below 0.2, which verified the excellent stability of Ln@Fe NPs. The high-resolution TEM (HRTEM) showed the lattice fringes with a d-spacing of 0.51 nm, corresponding to the (1 0 0) planes of the LnNPs (Fig. 1b). The core-multishell structure of Ln@Fe NPs was further confirmed by high-angle annular dark-field scanning transmission electron microscopy (HAADF-STEM) and the shell thickness from the inside to the outside (S1-S3) is 10.52 nm, 14.79 nm, and 6.37 nm, respectively (Fig. 1c). Elemental mapping (Fig. S3) of the Ln@Fe NPs showed the presence of the major elements, including Er^{3+} in the core ($NaErF_4$:2%Ce), Yb^{3+} in the subouter layer ($NaYbF_4$:0.5 %Tm), and Fe^{3+} in the outermost layer. Moreover, energy-dispersive X-ray spectroscopy (EDX) also confirmed similar element composition in the Ln@Fe NPs, and the weight ration of Ln and Fe element was
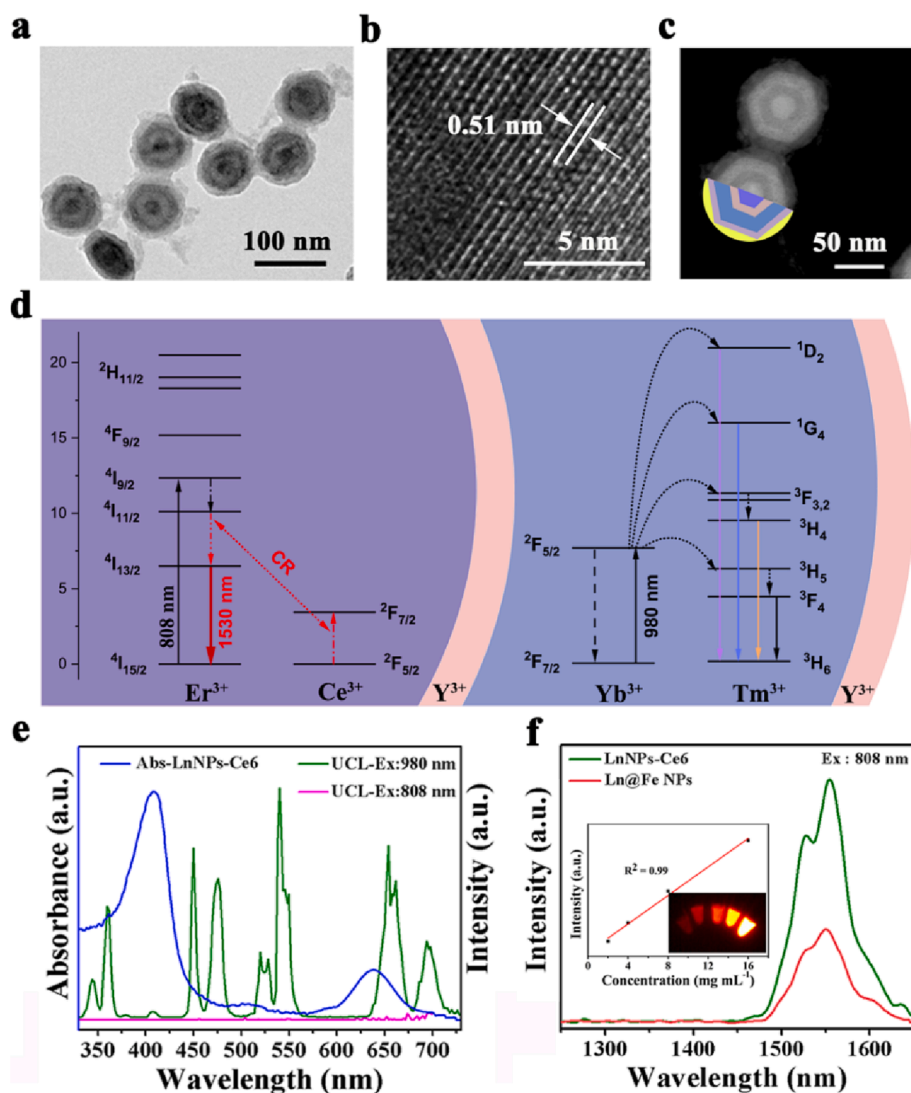
Fig. 1. Characterisation of Ln@Fe NPs. (a) TEM and (b) HRTEM images of Ln@Fe NPs. (c) HAADF-STEM image of Ln@Fe NPs. (d) Schematic of the luminescence mechanism of LnNPs triggered by 808 and 980 nm, respectively. (e) UV–vis absorption spectra of LnNPs-Ce6 (blue line) and upconversion emission spectrum of LnNPs with the 808 nm (pink line) and 980 nm (green line). (f) Downshifting emission spectrum of LnNPs-Ce6 (green line), Ln@Fe NPs (red line), and *in vitro* NIR-IIb imaging of Ln@Fe NPs at different concentrations (inset) upon irradiation at 808 nm.

determined to be 59.83% and 3.58%, respectively (Fig. S4).

The luminescent mechanism of LnNPs was illustrated in Fig. 1d. When the 808 nm excitation is switched on, the $^4I_{9/2}$ of Er^{3+} ions in core were populated and then the electrons transitioned to $^4I_{11/2}$ due to the non-radiation relaxation. With the existence of Ce^{3+} ions, the cross relaxation process ($^4I_{11/2}$ (Er^{3+}) + $^2F_{7/2}$(Ce^{3+})→$^4I_{13/2}$ (Er^{3+}) + $^2F_{5/2}$(Ce^{3+})) between Er^{3+} and Ce^{3+} ions greatly enhanced the population of $^4I_{11/2}$ energy level, resulting in a considerable 1530 nm emission for NIR-IIb imaging. Meanwhile, when the excitation source was switched to 980 nm, the NaYF$_4$:Yb/Tm shell could absorb 980 nm excitation energy, resulting in obviously bule-UV (362 nm, 482 nm) emission which could provide the possibility to active the coupling photosensitizers-Ce6 for PDT. Then, the successful conjugation of Ce6 to NH$_2$-modified LnNPs was verified by the typical absorption spectra of Ce6 (Fig. 1e, blue line) and fluorescence spectra (λex = 404 nm) (Fig. S5) of LnNPs-Ce6. The absorption spectra of Ce6 overlapped with the UCL of LnNPs (Fig. 1e, green line), which indicated the possibility of energy transfer between Ce6 and LnNPs (λex = 980 nm). And it was measured that each LnNPs was coupled with 144 molecules of Ce6. Almost no UCL was observed upon switching to the imaging function (λex = 808 nm), but 1550 nm downshifting emission was attenuated, suggesting the excellent decoupling theranostic performance of imaging-guided PDT (Fig. 1f). Furthermore, the NIR-IIb imaging profiles of Ln@Fe NPs were evaluated (Fig. 1f, inset) at different concentrations, and nanoparticle concentration-dependent downshifting emission intensity demonstrated the optical stability of Ln@Fe NPs, revealing the possibility for NIR-IIb imaging *in vivo*.

3.2. Photothermal performance and ROS generation capacity of Ln@Fe NPs

Next, we explored the TME-activatable ROS generation of Ln@Fe NPs (Fig. 2a). After coating with the Fe-GA shell, a strong photo-absorption was observed in the NIR-II region of the absorption spectra of Ln@Fe NPs, suggesting PTT potential (Fig. S6), and the changed color also confirmed it (Fig. 2b, inset). In addition, the absorption intensity of Ln@Fe NPs increased with the increasing proportion of GA in the Fe-GA shell (Fig. 2b), which indicated that the photothermal performance of Ln@Fe NPs could be optimized by adjusting the Fe/GA feeding ratio. To study its photothermal effect, Ln@Fe NPs solutions were exposed to a 1064 nm laser (1 W cm^{-2}) for 10 min. The temperature change was recorded by the thermal imaging system every 30 s. As shown in Fig. S7 and S8, the solution temperature of Ln@Fe NPs gradually increased over time. The maximum photothermal conversion efficiency (PCE) of 40.3% was achieved when the mass feeding ratio of Fe: GA was 1:0.2 (Fig. S9); thus, we chose this feeding ratio for subsequent experiments. Notably, after coating with the Fe-GA complex, the multiple upconversion emissions of LnNPs were significantly quenched, as shown in Fig. 2c. Thanks to the acid responsive-decomposition behavior of Fe-GA (low pH presents fewer coordination numbers) [36], the acidic conditions induced the release of Fe^{3+} and GA from the Ln@Fe NPs, turning "ON" the PDT effect (UCL recovery). Therefore, the time-dependent release profile of Fe^{3+} was evaluated by monitoring the changes in UCL at different pH values (5, 6.5, and 7.4). As expected, the quenched UCL was rapidly restored by 49.1% and 70.0% at pH 6.5 and pH 5, respectively, within 2 h, while negligible UCL recovery was detected at pH 7.4
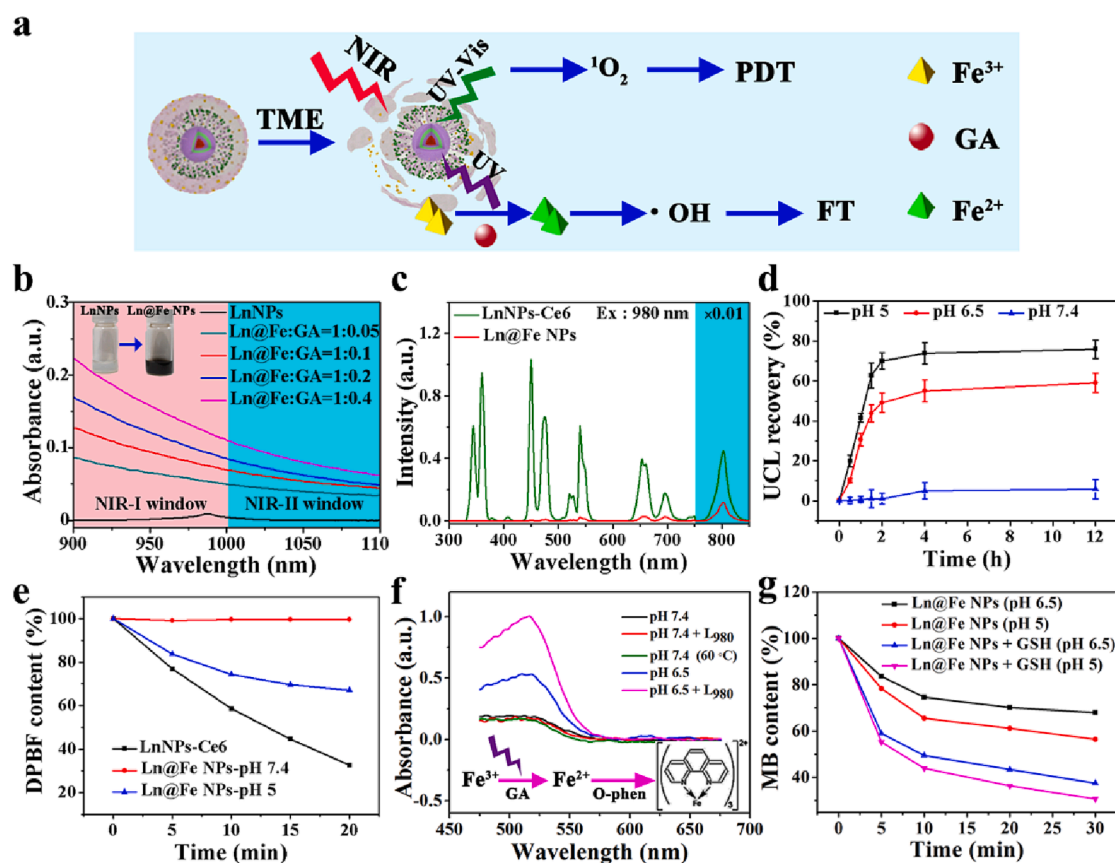

Fig. 2. Characterization of photothermal performance and ROS generation ability of Ln@Fe NPs. (a) Schematic illustration of TME-activatable ROS generation. (b) Absorption spectrum of Ln@Fe NPs with different ratios of Fe and GA. Digital photographes of LnNPs before (left) and after (right) coating with Fe-GA shell (inset). (c) UCL spectra of LnNPs-Ce6 before and after coating with the Fe-GA complex. (d) UCL recovery profiles of Ln@Fe NPs at different pH values. (e) Time-dependent absorbtance of DPBF at 417 nm in different pH values under 980 nm excitation. (f) Absorption spectrum of o-phenanthroline-Fe^{2+} after different treatments. (g) The degradation rate curves of MB induced by Ln@Fe NPs with different treatments (H$_2$O$_2$: 10 mM and GSH: 10 mM).

(Fig. 2d), indicating the excellent stability of Ln@Fe NPs under neutral physiological conditions. As shown in Fig. S10, the ratio of emission intensity of Ln@Fe NPs between different wavelengths (e.g., I_{450}/I_{650} at pH 5 was 1.43- and 2.87 fold of the values at pH 6.5 and pH 7.4 after 2 h treatment, respectively. As shown in Fig. S11, the change in the temperature (ΔT) upon irradiation at 1064 nm laser was significantly reduced under acidic conditions (pH = 5 and 6.5), while there was only a negligible decrease at pH 7.4, which further confirmed the pH-responsive nature of Ln@Fe NPs.

To investigate the photodynamic properties of Ln@Fe NPs upon 980 nm irradiation, the $^1O_2$ production profiles were studied using 1,3-diphenylisobenzofuran (DPBF) as a probe at different pH environments. The absorbance of DPBF was significantly reduced (76.4%) after the LnNPs-Ce6 were irradiated for 20 min (Fig. 2e, black line), indicating that LnNPs-Ce6 possessed photosensitive characteristics. Besides, almost no DPBF was degraded when the Ln@Fe NPs were under physiological conditions at pH 7.4, indicating that the Fe-GA complex blocked the PDT effect. After the Ln@Fe NPs were treated at pH 5 buffer solution for 2 h, the degradation rate of DPBF was up to 33.4% (Fig. 2e), which indicated the effective generation of $^1O_2$ owing to the recovery of UCL mediated by the released Fe^{3+} (namely pH-activated PDT).

1,10-phenanthroline was used to detect UV emission and GA-induced transformation of Fe^{3+} to Fe^{2+}. Fig. 2f showed a typical characteristic peak (510 nm) when the Ln@Fe NPs were treated at pH 6.5 buffer solution for 2 h due to the GA-induced reduction of Fe^{3+} to Fe^{2+}. Similarly, with the irradiation of 980 nm light, the absorption intensity at 510 nm had been significantly improved, but there was no obvious change in the 60 °C, confirming the UV-photo-reduction of Fe^{3+} to Fe^{2+}. The •OH production was measured using methylene blue (MB) as a probe against different pH values (5 or 7.4). After treatment with Ln@Fe NPs, the absorbance of MB decreased by 43.6% (pH 5) and 32.1% (pH 6.5), respectively (Fig. 2g). Additionally, in the presence of GSH (10 mM), the degradation of MB was significantly enhanced (69.3% in pH 5 and 62.5% in pH 6.5), likely due to the reduction of Fe^{3+} into Fe^{2+} by GSH for further participation in the Fenton reaction, thereby enhancing the generation of •OH. Taken together, Ln@Fe NPs can perturb
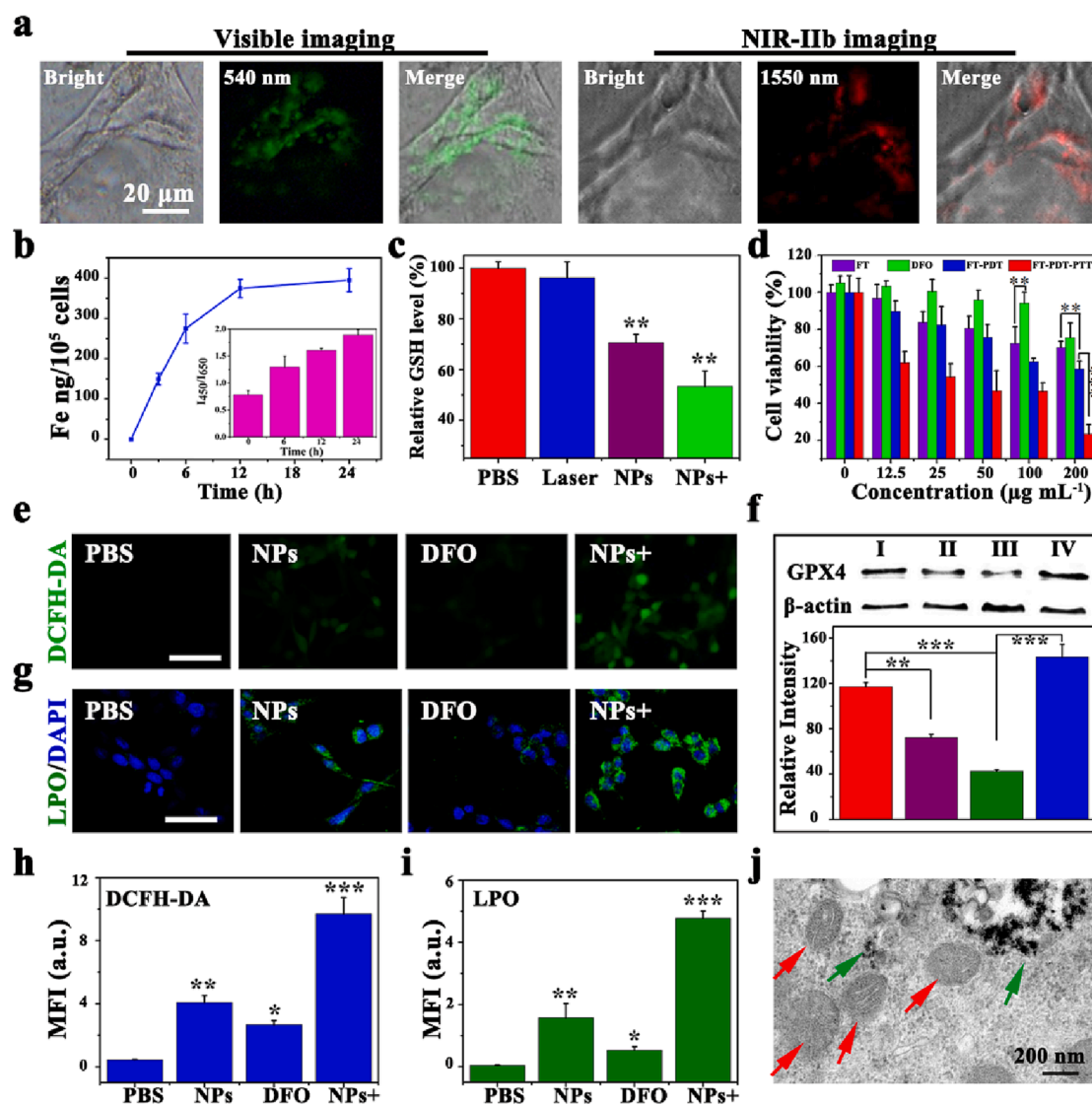
Fig. 3. Cellular internalization and cytotoxicity of Ln@Fe NPs against 4 T1 cells. (a) CLSM images and NIR-IIb microscopy images of 4 T1 cells incubated with Ln@Fe NPs. Scale bar: 20 μm. (b) Quantitative analysis of intracellular iron content and UCL intensity ratio of I_{450}/I_{650} (inset) intracellular LnNPs at different incubation time. (c) Intracellular levels of GSH in 4 T1 cells after different treatments. (d) Viability of 4 T1 cells after different treatments. (e) DCFH-DA and (g) liperfluo probe staining of 4 T1 cells after different treatments. Scale bar: 50 μm. (f) GPX4 expression in 4 T1 cells treated with PBS (I), Ln@Fe NPs (II), Ln@Fe NPs + $L_{980+1064}$ (III), and Ln@Fe NPs + DFO (IV). Intracellular (h) ROS and (i) LPO intensity after different treatments. (j) Bio-TEM image of 4 T1 cells after treatment with Ln@Fe NPs. The green arrows indicate the Ln@Fe NPs ingested by cells and the red arrows refer to the mitochondria. *P < 0.05, **P < 0.01, ***P < 0.001.

intracellular redox homeostasis by boosting ROS generation and GSH depletion.

3.3. Cellular uptake and in vitro therapeutic efficiency of Ln@Fe NPs

The cellular uptake of Ln@Fe NPs was studied in 4 T1 breast tumor cells. After incubation with Ln@Fe NPs for 6 h, the intracellular green UCL (540 nm) and downshifting emission (1550 nm) were detected, respectively (Fig. 3a). In addition, the results from inductively coupled plasma mass spectrometry (ICP-MS) showed that the content of intracellular Fe increased over time (Fig. 3b), demonstrating that Ln@Fe NPs were efficiently internalized by 4 T1 cells. Intracellular Fe^{3+} release was determined by the variation in the UCL of LnNPs. As shown in Fig. 3b (inset), the UCL ratio (I_{450}/I_{650}) increased with a longer incubation time from 0 to 24 h, which suggested that Fe^{3+} was released from the Ln@Fe NPs that were internalized by 4 T1 cells. The FerroOrange probe was used to detect intracellular Fe^{2+} level. Fig. S12 shows that the intracellular red fluorescence signal gradually increased within 24 h. The quantitative results demonstrated that the mean fluorescence intensity at 24 h was 3.28-fold more than at 0 h, indicating the increase in Fe^{2+} level, which is essential for the generation of •OH. 2,7-dichlorofluorescin diacetate (DCFH-DA) was used to evaluate the generation of ROS after different treatments. As shown in Fig. 3e, treatment with Ln@Fe NPs induced higher ROS levels than the control treatment (PBS). ROS generation was lower in the presence of deferoxamine mesylate (DFO, iron ion chelator), demonstrating that the ROS signal was attributed to the •OH generated by Fe^{3+}/Fe^{2+}-mediated Fenton reaction. Furthermore, 4 T1 cells treated with Ln@Fe NPs had a bright green fluorescence signal under laser irradiation (0.6 W cm^{-2}, 6 min), indicating that the intracellular ROS concentration was significantly elevated, which could mainly be attributed to the $^1O_2$ generated by 980 nm light-triggered PDT and intracellular hyperthermia (PTT)-enhanced ROS generation. Quantification of the fluorescence signals revealed that the ROS level in the NPs + group was 2.38 times higher than that in the NPs group (Fig. 3h).

In order to verify the role of GSH consumption in reducing Fe^{3+} to Fe^{2+}, the intracellular level of GSH was measured after different treatments. Compared with the PBS group, the intracellular GSH levels in the NPs and NPs + groups were lower by 29.4% and 46.7%, respectively (Fig. 3c). GSH consumption not only enhances ROS-mediated oxidative damage but also inactivates the GPX4, further augmenting intracellular LPO that results in ferroptosis [37,38]. Fig. 3f shows the expression level of GPX4, which was down-regulated by 38.5% after treatment with Ln@Fe NPs. With the assistance of NIR light (L$_{980+1064}$), GPX4 expression was further suppressed (63.2%), owing to enhanced ROS production. As shown in Fig. 3g, in contrast to the PBS group, cells treated with Ln@Fe NPs exhibited stronger green fluorescence, and reduced green fluorescence was observed in the presence of DFO (Fig. 3i), which confirmed the close association of LPO accumulation with Ln@Fe NPs-mediated ferroptosis pathway. The bio-TEM image (Fig. 3j) indicated that the majority of the Ln@Fe NPs were located within the lysosomes, and some escaped from lyso/endosomes after degradation. More importantly, the mitochondria were swollen, and the ridges disappeared, which are typical characteristics associated with ferroptosis, validating Ln@Fe NPs-mediated effective ferroptosis [39,40].

The cytotoxicity of Ln@Fe NPs was verified through CCK-8 assay. As shown in Fig. 3d, the viability of Ln@Fe NPs-treated 4 T1 cells gradually decreased dose-dependent, which was attenuated upon incubation with DFO, indicating that the cytotoxicity was caused by Fe^{3+}/Fe^{2+}-mediated ferroptosis [41]. Specifically, the 4 T1 cell viability decreased by 25% after incubation with Ln@Fe NPs (200 μg mL^{-1}), while there was no obvious toxicity on normal cells (mouse fibroblast cells, L929) (Fig. S13), indicating that cancer cells are more sensitive to ferroptosis. In addition, co-irradiation with 980 nm and 1064 nm laser with safe optical power density resulted in significant cell death (~77%, FT-PDT-PTT) compared to the group with only 980 nm laser irradiation (~42%,

FT-PDT). The above results confirmed the synergistic effect of PTT-PDT-FT. Such synergistic cytotoxic effect of PTT/PDT/FT was further confirmed by live/dead discrimination using the calcein-AM (green fluorescence) and propidium iodide (PI, red fluorescence) double stain kit. No obvious cell damage (red fluorescence) was observed in the PBS group (Fig. S14). However, after treatment with Ln@Fe NPs, the number of dead cells was increased, and almost all the cells died in the Ln@Fe NPs + group, which suggested the synergistic therapeutic effect of PTT/PDT/FT. Lyso-Tracker Red was used to evaluate the effect of different treatments on the lysosome. As shown in Fig. S15, the red-stained spots were visible in the cytoplasm in the PBS group. However, red fluorescence signal was detected in the entire cytoplasm, implying that lysosomes were destroyed when the cells were treated with Ln@Fe NPs + L$_{980+1064}$ [42]. The above results fully demonstrated the potential of Ln@Fe NPs-mediated synergistic therapeutic effects *in vitro*.

3.4. ICD stimulation induced by PTT/PDT/FT

To investigate the *in vitro* ICD effects induced by Ln@Fe NPs-mediated synergistic therapy, crucial cellular markers of ICD (CRT, HMGB1 and ATP) were measured [43,44]. Cells that undergo ICD tend to expose CRT on the cell surface as an "eat me" signal to activate the immune response [45,46]. Among the treatment groups, the CRT exposure level was highest in the synergistic treatment (NPs +) group, about 2 times that in the NPs-treated group (Fig. 4a-b). This might be induced by ROS and hyperthermia-mediated stress. Extracellular release of HMGB1 is often associated with cell death, and the released HMGB1 binds with antigen-presenting cells (APCs), leading to the expression and secretion of inflammatory cytokines that promote DCs maturation. Consistently, the up-regulated level of HMGB1 and down-regulated level of intracellular ATP were found in the NPs + group (Fig. 4c and S16), which indicated that Ln@Fe NPs mediated-PTT/PDT/FT effectively induced ICD through multiple pathways. Next, a transwell assay was conducted to evaluate the ICD-induced maturation of DCs (Fig. 4d). The synergistic treatment (NPs +) group displayed the highest levels of secreted inflammatory cytokines (interleukin-6 (IL-6) and tumor necrosis factor-α (TNF-α)) from DCs (Fig. 4e-f). Flow cytometry analysis revealed that Ln@Fe NPs significantly promoted the maturation of DCs (CD80$^+$CD86$^+$) (23.3%), which could probably attribute to Ln@Fe NPs-mediated ferroptosis [47]. Meanwhile, the proportion of mature DCs was further up-regulated in the NPs + group (30.9%) (Fig. 4g). Overall, Ln@Fe NPs-mediated synergistic therapy through PTT/PDT/FT effectively induced ICD and promoted the maturation of DCs, which are known to evoke potential immune responses in the host.

3.5. NIR-IIb/PA dual modal imaging in vivo

Before conducting *in vivo* experiments, hemolysis assay was performed. As shown in Fig. S17, there was almost no hemolysis within the detection concentration range (0–400 μg mL^{-1}), suggesting the excellent biosafety of Ln@Fe NPs. In vivo real-time NIR-IIb and PA imaging were performed to visualize the accumulation of Ln@Fe NPs in the tumor sites. As shown in Fig. 5a, the whole-body vascular system, especially the tumor blood supply network, was clearly observed with a 1500 nm long-pass (LP) filter at 5 min post-intravenous injection of Ln@Fe NPs. Moreover, Gaussian-fitting of the cross-sectional intensity of blood vessels near the tumor site was applied. As a result, the full width at half-maximum (FWHM) values of the corresponding blood vessels were 310 μm and 210 μm, respectively (Fig. 5b), confirming that the imaging quality of Ln@Fe NPs was equivalent to that of other NIR-IIb agents [48,49]. Subsequently, the enrichment profiles of Ln@Fe NPs at the tumor sites were measured over time. As shown in Fig. 5c-e, the NIR-IIb luminescence signals at the tumor area gradually increased from 0.5 h to 4 h and reached a maximum at 4 h post-injection owing to the enhanced permeability and retention (EPR) effect. In addition to the tumor site, most Ln@Fe NPs accumulated in the liver and spleen (Fig. S18a-d). The
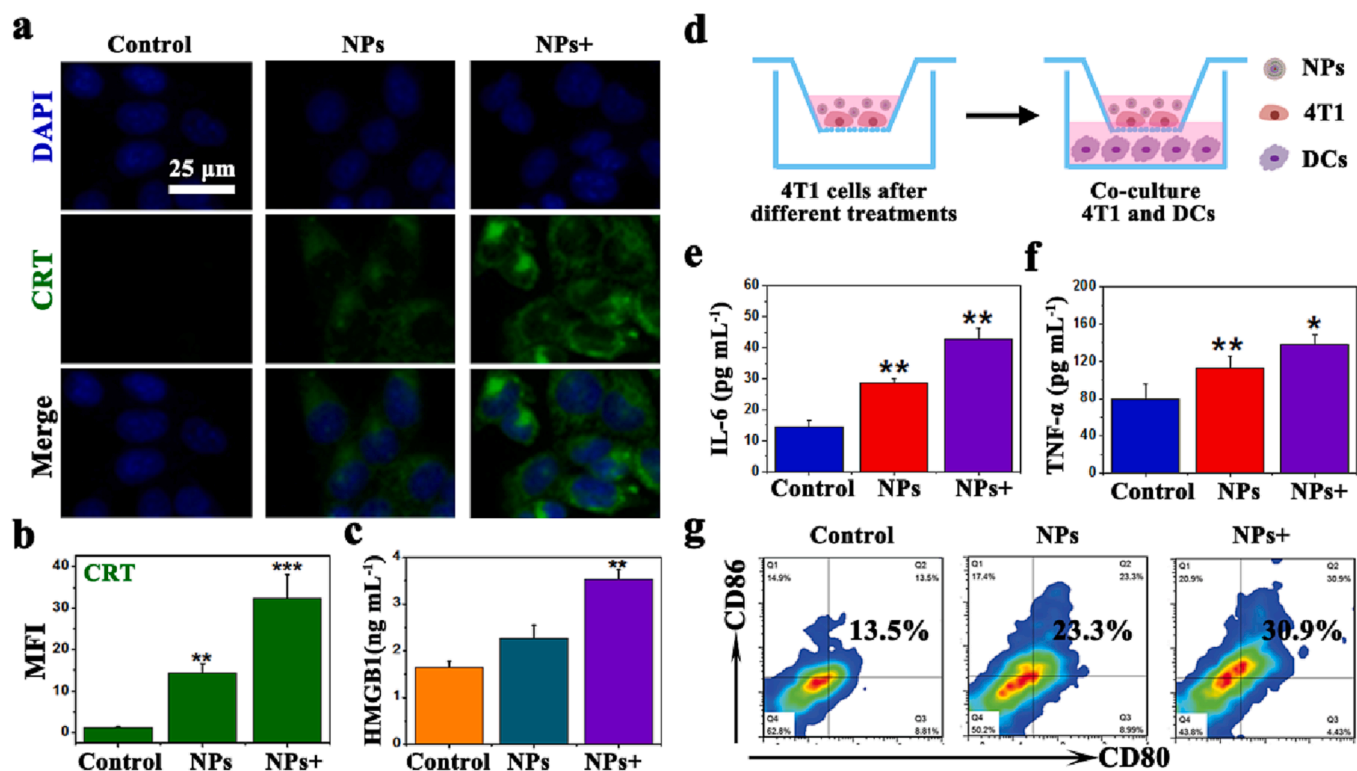
Fig. 4. In vitro evaluation of ICD. (a) Immunofluorescence staining images of CRT and (b) mean fluorescence intensity (MFI) of 4 T1 cells after different treatments. (c) HMGB1 levels in the supernatant. (d) Schematic illustration of the Transwell system. The content of IL-6 (e) and TNF-α (f) in supernatant of DCs. (g) Flow cytometry assay results showing effects on DCs maturation from different treatment groups (gated on CD11c$^+$ cells). Data were represented as mean ± SD (n = 3). *P < 0.05, **P < 0.01, and ***P < 0.001.
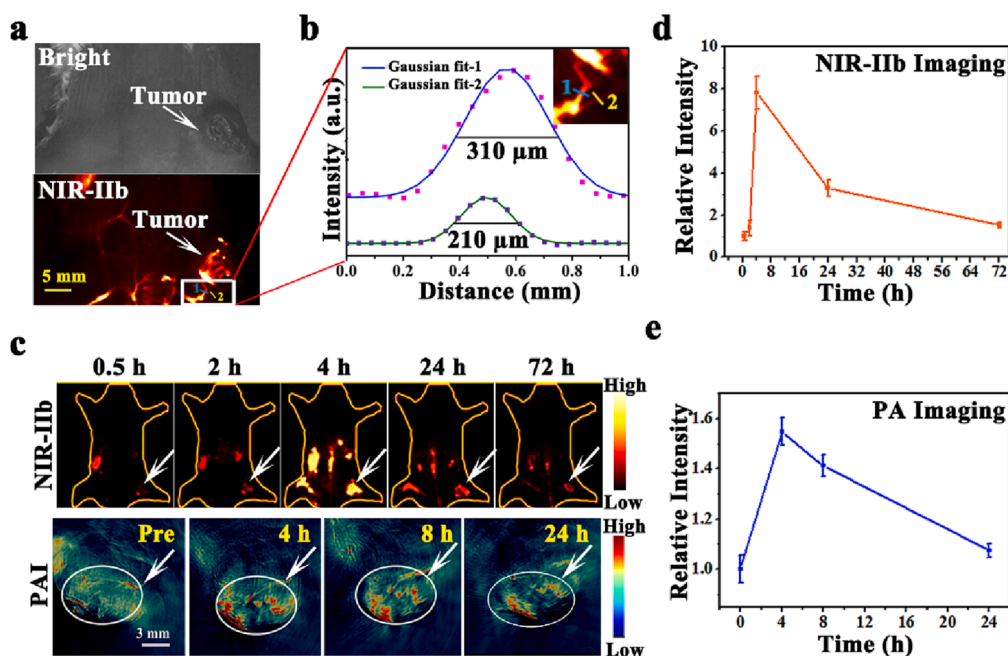

Fig. 5. NIR-IIb and PA imaging of Ln@Fe NPs *in vivo*. (a) NIR-IIb vascular imaging. (b) Gaussian-fitting of the cross-sectional intensity of blood vessels in the tumor site. (c) In vivo NIR-IIb and PA images of 4 T1 tumor-bearing mice before and after intravenous injections with Ln@Fe NPs at different points (white arrows refer to the tumor site). (d) The relative change in NIR-IIb and (e) PA signal intensities at the tumor site after intravenous injection of Ln@Fe NPs.

fluorescence images showed that the luminescence signal of Ln@Fe NPs in spleen gradually increased after administration and peaked at 24 h, then gradually weakened over time. The luminescence signal of liver peaked at 2 h after administration and decreased with time, indicating the typical hepatobiliary and spleen clearance of the nanoparticles. Besides, we also conducted NIR-IIb imaging of mouse feces after administration. As shown in Fig. S19a, the luminescence signals of LnNPs could be detected in the feces after administration. The

degradation profiles of Ln@Fe NPs were also studied by quantifying the main elements in feces, such as Yb, Y, and Er, with inductively coupled plasma mass spectrometry (ICP-MS) characterization. It was found that the relative content ratio of Ln element in feces did not show significant changes within 5 days, which is consistent with the EDX results (Fig. S19b). These results indicated that Ln@Fe NPs could be excreted through the typical hepatobiliary pathway, and LnNPs were almost not degraded. In addition, the pharmacokinetics was investigated by i.v. injection of Ln@Fe NPs (50 mg/kg) and followed by collecting blood at different time points. The half-life of Ln@Fe NPs in blood circulation was approximately 7 min (Fig. S20).

Additionally, PA signals in the tumor regions were enhanced over time and peaked at 4 h post-injection, 1.55-fold stronger than at pre-injection. Subsequently, the PA signals were gradually reduced to the pre-injection level 24 h post-injection, implying that the Ln@Fe NPs displayed strong PA performance. These results demonstrated the feasibility of NIR-IIb/PA dual-modal imaging-guided synergistic

therapy. Considering the maximum enrichment time of Ln@Fe NPs at the tumor site, laser irradiation ($L_{980+1064}$) was applied at 4 h post-injection for antitumor therapy (derived from the G4 treatment group, see Treatment section).

3.6. Evaluation of the antitumor efficacy and ICD effect of Ln@Fe NPs in vivo

Next, we evaluated the *in vivo* antitumor effects of Ln@Fe NPs-mediated synergistic therapy (Fig. 6a). 4 T1 tumor-bearing mice were randomly divided into four groups (n = 4 for each group) and treated as follows: saline (G1); saline + $L_{980+1064}$ (G2); Ln@Fe NPs (G3); and Ln@Fe NPs + $L_{980+1064}$ (G4). Thanks to the excellent photothermal conversion capacity of Ln@Fe NPs, the tumor temperature rapidly increased and reached up to 53.1 °C within 10 min in the Ln@Fe NPs + $L_{980+1064}$ group, which indicated that Ln@Fe NPs were suitable for *in vivo* PTT (Fig. S21). Notably, the phototherapy triggered by laser
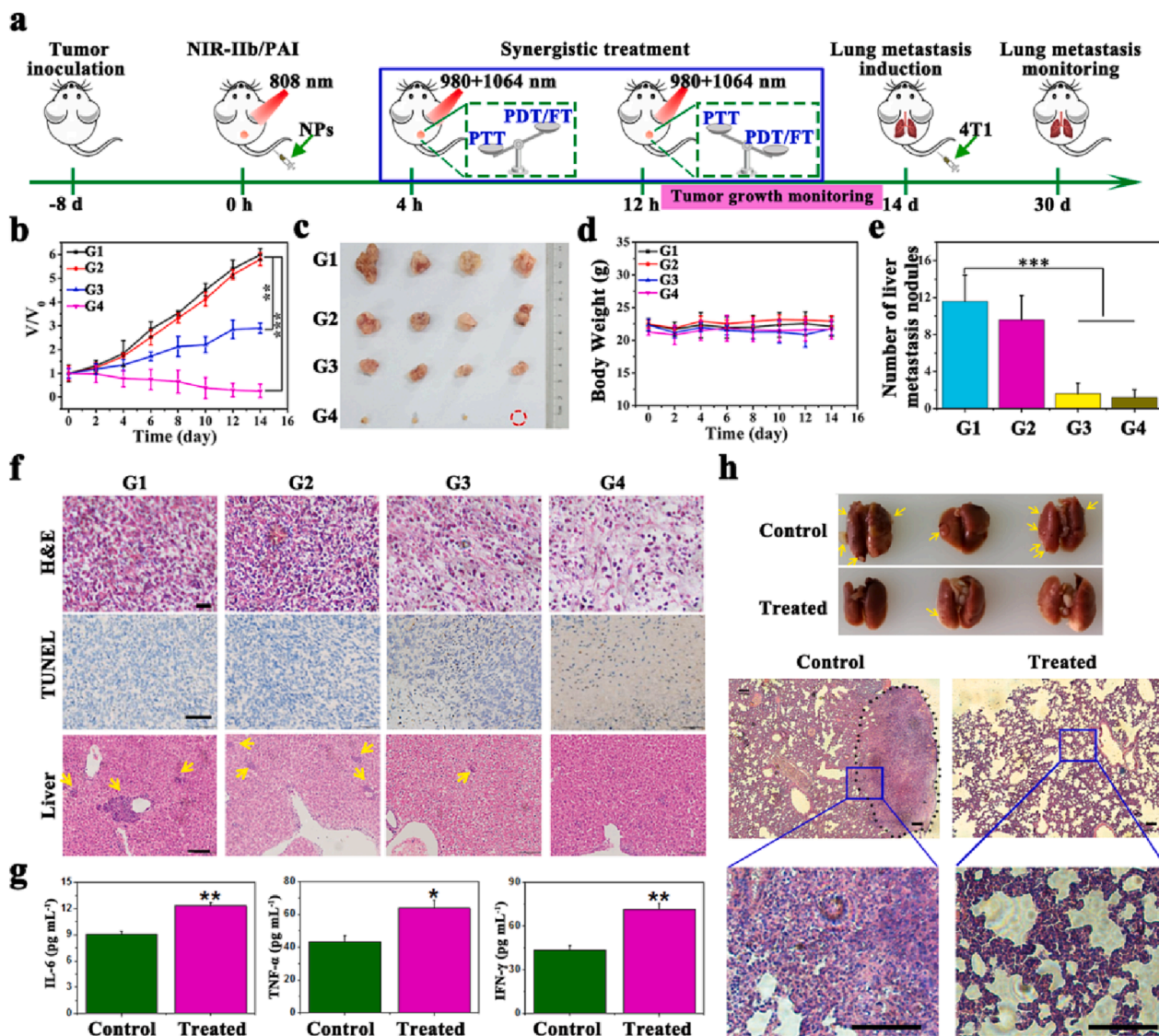
Fig. 6. Evaluations of the *in vivo* antitumor effects of Ln@Fe NPs. (a) Schematic illustration of treatment schedules for anticancer therapy with Ln@Fe NPs (10 mg kg^{-1}). (b) Changes in the relative tumor volumes in the different groups with different treatments. (c) Photos of tumor tissues after different treatments (n = 4). (d) Change in the body weight of animals from different groups during treatment. (e) Number of metastatic lesions in livers from mice after different treatments. (f) H&E and TUNEL staining of tumor sections and H&E staining of metastatic liver nodules after different treatments. Yellow arrows indicate metastatic lesions. Scale bar: 100 μm. (g) Levels of the inflammatory cytokines (IL-6, TNF-α, and IFN-γ) in the serum after the treatment of 7th day. (h) Representative photographs and H&E staining of lung tissues on day 30. Scale bar: 100 μm. (G1: saline, G2: saline + $L_{980+1064}$, G3: Ln@Fe NPs, G4: Ln@Fe NPs + $L_{980+1064}$). Data were represented as mean ± SD (n = 4). *P < 0.05, **P < 0.01, and ***P < 0.001.

irradiation can simultaneously achieve a precise tumor treatment under real-time NIR-IIb imaging guidance. After photoirradiation, the tumor volume and body weight of mice were monitored every two days. As presented in the tumor growth curves, a certain degree (51.7%) of tumor inhibition was achieved in the Ln@Fe NPs (blue line) group, which was attributed to the Ln@Fe NPs-mediated ferroptosis. Nevertheless, Ln@Fe NPs alone did not inhibit tumor growth completely. Combined with photoirradiation, we achieved almost complete tumor eradication ($\approx$ 98%) (Fig. 6b-pink line), indicating the vastly improved synergistic therapeutic performance of PTT/PDT/FT. The photograph of the dissected tumors visually reveals the strong antitumor effects (Fig. 6c). There was no significant fluctuation in the bodyweight of mice belonging to all groups during the treatment period (Fig. 6d), which indicated the good biocompatibility of the Ln@Fe NPs. Furthermore, hematoxylin and eosin (H&E) and terminal dUTP-mediated nick-end labeling (TUNEL) staining of the tumor sections also indicated that most severe histological damages and apoptotic cells were present in the Ln@Fe NPs + $L_{980+1064}$ group (Fig. 6f). This result was consistent with tumor growth inhibition rate, which further confirmed that the combination of Ln@Fe NPs with NIR laser irradiation was effective in killing the tumor cells. After the treatment, multiple metastatic sites were detected in the livers of saline-treated mice or photoirradiated mice due to the rapid metastasis of 4 T1 cells. Encouragingly, fewer metastatic lesions were observed in the Ln@Fe NPs treated group and almost no metastatic lesions were found in mice treated with Ln@Fe NPs combined with laser irradiation (Fig. 6e). These results demonstrated that Ln@Fe-mediated synergistic therapy effectively inhibited tumor metastasis, which might further benefit from the activation of the immune response [50]. Therefore, the immunological response was further investigated, including T cells infiltration and cytokine release. The levels of cytokines (IL-6, TNF-α, and IFN-γ) were significantly elevated in the serum (Fig. 6g). In addition, immunofluorescence staining of the tumor sections demonstrated that the synergistic treatment effectively promoted the activation and infiltration of $CD4^+/CD8^+$ T cells into the tumor tissues (Fig. S22). To further evaluate the anti-metastatic effects, the mice were rechallenged with intravenous injection of 4 T1 cells. As shown in Fig. 6h, obvious pulmonary metastases were detected in the control group. In contrast, there were fewer metastatic lesions in the treated group, which was further confirmed by H&E staining. These results demonstrated that Ln@Fe NPs-mediated synergistic therapy was able to induce strong antimetastatic effects by activating the immune response. Besides, there were no apparent histological abnormalities in other major organs in the mice (Fig. S23), validating the excellent biocompatibility and biosafety of Ln@Fe NPs.

4. Conclusion

In summary, we developed a ROS nanogenerator-Ln@Fe NPs, which could evoke antitumor immunity by amplifying intracellular oxidative stress. In the acidic TME, Fe-GA could be decomposed to release Fe^{3+}, which provides the iron source for FT. Upon NIR irradiation, on the one hand, the UV photons from Ln@Fe NPs induced the reduction of Fe^{3+} to Fe^{2+} and then participated in the Fenton reaction to promote the generation of •OH. On the other hand, the UV–Vis emission activated the coupling photosensitizer-Ce6, which triggers the generation of another ROS- $^1O_2$ for PDT. In addition, Fe-GA endows the Ln@Fe NPs with PTT performance. Both *in vivo* and *in vitro* experiments demonstrated that the above cooperative treatment strategy effectively triggered ICD by boosting ROS generation, and ultimately inhibited the occurrence of lung metastasis. Additionally, Ln@Fe NPs exhibited NIR-IIb downshifting emission upon 808 nm excitation, which can achieve non-destructive real-time NIR-IIb luminescence imaging-guided synergistic therapy. Overall, the current study demonstrates the feasibility and effectiveness of Ln@Fe NPs-based synergistic treatment to stimulate antitumor immunity, providing a new paradigm for developing theranostic agents.

Declaration of Competing Interest

The authors declare that they have no known competing financial interests or personal relationships that could have appeared to influence the work reported in this paper.

Data availability

I have shared the link to my data at the Attach File step

Appendix A. Supplementary data

Supplementary data to this article can be found online at https://doi.org/10.1016/j.cej.2023.143827.

References

[1] Z. Lu, S. Bai, Y. Jiang, S. Wu, D. Xu, Y. Chen, Y. Lan, Y. An, J. Mao, X. Liu, G. Liu, Porphyrin-based covalent organic framework for imaging guided cancer combinatorial immuno-sonodynamic therapy, Adv. Funct. Mater. 32 (2022) 2207749.

[2] D.M. Pardoll, The blockade of immune checkpoints in cancer immunotherapy, Nat. Rev. Cancer 12 (2012) 252–264.

[3] C. June, R. O'Connor, O. Kawalekar, S. Ghassemi, M. Milone, CAR T cell immunotherapy for human cancer, Science 359 (2018) 1361–1365.

[4] M. Lin, J. Svensson-Arvelund, G. Lubitz, A. Marabelle, I. Melero, B. Brown, J. Brody, Cancer vaccines: the next immunotherapy frontier, Nat. Cancer 3 (2022) 911–926.

[5] P.S. Hegde, D.S. Chen, Top 10 challenges in cancer immunotherapy, Immunity 52 (1) (2020) 17–35.

[6] A. Smole, A. Benton, M.A. Poussin, M.A. Eiva, C. Mezzanotte, B. Camisa, B. Greco, P. Sharma, N.G. Minutolo, F. Gray, A.S. Bear, M.L. Baroja, C. Cummins, C. Xu, F. Sanvito, A.L. Goldgewicht, T. Blanchard, A. Rodriguez-Garcia, M. Klichinsky, C. Bonini, C.H. June, A.D.P. Posey, G.P. Linette, B.M. Carreno, M. Casucci, D.J. P. Powell, Expression of inducible factors reprograms CAR-T cells for enhanced function and safety, Cancer Cell 40 (2022) 1470–1487.

[7] R. Vonderheide, K. Nathanson, Immunotherapy at large: the road to personalized cancer vaccines, Nat. Med. 19 (2013) 1098–1100.

[8] G. Kroemer, C. Galassi, L. Zitvogel, L. Galluzzi, Immunogenic cell stress and death, Nat. Immunol. 23 (4) (2022) 487–500.

[9] Z. Huang, D. Yao, Q. Ye, H. Jiang, R. Gu, C. Ji, J. Wu, Y. Hu, A. Yuan, Zoledronic acid-gadolinium coordination polymer nanorods for improved tumor radioimmunotherapy by synergetically inducing immunogenic cell death and reprogramming the immunosuppressive microenvironment, ACS Nano 15 (5) (2021) 8450–8465.

[10] Y. Chen, P. He, D. Jana, D. Wang, M. Wang, P. Yu, W. Zhu, Y. Zhao, Glutathione-depleting organic metal adjuvants for effective NIR-II photothermal immunotherapy, Adv. Mater. 34 (2022) 2201706.

[11] W. Li, J. Yang, L. Luo, M. Jiang, B. Qin, H. Yin, C. Zhu, X. Yuan, J. Zhang, Z. Luo, Y. Du, Q. Li, Y. Lou, Y. Qiu, J. You, Targeting photodynamic and photothermal therapy to the endoplasmic reticulum enhances immunogenic cancer cell death, Nat. Commun. 10 (2019) 3349.

[12] R. Lima-Sousa, B. Melo, C. Alves, A. Moreira, A. Mendonça, I. Correia, D. Melo-Diogo, Combining photothermal-photodynamic therapy mediated by nanomaterials with immune checkpoint blockade for metastatic cancer treatment and creation of immune memory, Adv. Funct. Mater. 31 (2021) 2010777.

[13] L.u. Yao, M.-M. Zhao, Q.-W. Luo, Y.-C. Zhang, T.-T. Liu, Z. Yang, M. Liao, P. Tu, K.-W. Zeng, Carbon quantum dots-based nanozyme from coffee induces cancer cell ferroptosis to activate antitumor immunity, ACS Nano 16 (6) (2022) 9228–9239.

[14] B. Nasseri, E. Alizadeh, F. Bani, S. Davaran, A. Akbarzadeh, N. Rabiee, A. Bahadori, M. Ziaei, M. Bagherzadeh, M. Saeb, M. Mozafari, M. Hamblin, Nanomaterials for photothermal and photodynamic cancer therapy, Appl. Phys. Rev. 9 (2022), 011317.

[15] S. Liang, C.Q. Sun, P.P. Yang, P.A. Ma, S.S. Huang, Z.Y. Cheng, X.F. Yu, J. Lin, Core-shell structured upconversion nanocrystal-dendrimer composite as a carrier for mitochondria targeting and catalase enhanced anti-cancer photodynamic therapy, Biomaterials 240 (2020), 119850.

[16] Y. Liu, Y. Liu, W. Bu, C. Cheng, C. Zuo, Q. Xiao, Y. Sun, D. Ni, C. Zhang, J. Liu, J. Shi, Hypoxia induced by upconversion-based photodynamic therapy: towards highly effective synergistic bioreductive therapy in tumors, Angew. Chem. Int. Ed. 54 (2015) 8105–8109.

[17] Y. Liu, W. Zhen, L. Jin, S. Zhang, G. Sun, T. Zhang, X. Xu, S. Song, Y. Wang, J. Liu, H. Zhang, All-in-one theranostic nanoagent with enhanced reactive oxygen species generation and modulating tumor microenvironment ability for effective tumor eradication, ACS Nano 12 (5) (2018) 4886–4893.

[18] B. Ding, J. Yue, P. Zheng, P. Ma, J. Lin, Manganese oxide nanomaterials boost cancer immunotherapy, J. Mater. Chem. B 9 (35) (2021) 7117–7131.

[19] H. Min, Y. Qi, Y. Zhang, X. Han, K. Cheng, Y. Liu, H. Liu, J. Hu, G. Nie, Y. Li, A graphdiyne oxide-based iron sponge with photothermally enhanced tumor-specific fenton chemistry, Adv. Mater. 32 (2020) 2000038.

[20] T. Szatrowski, C. Nathan, Production of large amounts of hydrogen-peroxide by human tumor-cells, Cancer Res. 51 (1991) 794–798.

[21] W. Wang, Z. Feng, B. Li, Y. Chang, X.u. Li, X.u. Yan, R. Chen, X. Yu, H. Zhao, G. Lu, X. Kong, J. Qian, X. Liu, Er^{3+} self-sensitized nanoprobes with enhanced 1525 nm downshifting emission for NIR-IIb in vivo bio-imaging, J. Mater. Chem. B 9 (12) (2021) 2899–2908.

[22] Y. Feng, H. Chen, Y. Wu, I. Que, F. Tamburini, F. Baldazzi, Y. Chang, H. Zhang, Optical imaging and pH-awakening therapy of deep tissue cancer based on specific upconversion nanophotosensitizers, Biomaterials 230 (2020), 119637.

[23] C. Bagot, E. Rappeport, A. Das, T. Tis, W. Park, True FRET-based sensing of ph via separation of FRET and photon reabsorption, Adv. Opt. Mater. 10 (2022) 2200242.

[24] J. Zhou, Q. Liu, W. Feng, Y. Sun, F. Li, Upconversion luminescent materials: advances and applications, Chem. Rev. 115 (1) (2015) 395–465.

[25] F. Li, Y. Du, J. Liu, H. Sun, J. Wang, R. Li, D. Kim, T. Hyeon, D. Ling, Responsive assembly of upconversion nanoparticles for ph-activated and near-infrared-triggered photodynamic therapy of deep tumors, Adv. Mater. 30 (2018) 1802808.

[26] Z. Zhang, J. Rahmat, R. Mahendran, Y. Zhang, Controllable assembly of upconversion nanoparticles enhanced tumor cell penetration and killing efficiency, Adv. Sci. 7 (2020) 2001831.

[27] H. Hu, H. Wang, Y. Yang, J. Xu, X. Zhang, A bacteria-responsive porphyrin for adaptable photodynamic/photothermal therapy, Angew. Chem. Int. Ed. 61 (2022) 202200799.

[28] X. Wei, C. Zhang, S. He, J. Huang, J. Huang, S. Liew, Z. Zeng, K. Pu, A dual-locked activatable phototheranostic probe for biomarker-regulated photodynamic and photothermal cancer therapy, Angew. Chem. Int. Ed. 61 (2022) 202202966.

[29] M. Wang, M. Chang, C. Li, Q. Chen, Z. Hou, B. Xing, J. Lin, Tumor-microenvironment-activated reactive oxygen species amplifier for enzymatic cascade cancer starvation/chemodynamic /immunotherapy, Adv. Mater. 34 (2022) 2106010.

[30] Y. Zhong, H. Dai, A mini-review on rare-earth down-conversion nanoparticles for NIR-II imaging of biological systems, Nano Res. 13 (5) (2020) 1281–1294.

[31] Y. Zhong, Z. Ma, S. Zhu, J. Yue, M. Zhang, A. Antaris, J. Yuan, R. Cui, H. Wan, Y. Zhou, W. Wang, N. Huang, J. Luo, Z. Hu, H. Dai, Boosting the down-shifting luminescence of rare-earth nanocrystals for biological imaging beyond 1500 nm, Nat. Commun. 8 (2017) 737.

[32] J. Duan, T. Liao, X. Xu, Y. Liu, Y. Kuang, C. Li, J., Metal-polyphenol nanodots loaded hollow MnO_2 nanoparticles with a "dynamic protection" property for enhanced cancer chemodynamic therapy, Colloid Interface Sci. 634 (2023) 836.

[33] H. Chen, F. Wu, X. Xie, W. Wang, Q. Li, L. Tu, B. Li, X. Kong, Y. Chang, Hybrid nanoplatform: enabling a precise antitumor strategy via dual-modal imaging-guided photodynamic/chemo-/immunosynergistic therapy, ACS Nano 15 (2021) 20643–20655.

[34] P. Zhang, Y.i. Hou, J. Zeng, Y. Li, Z. Wang, R. Zhu, T. Ma, M. Gao, Coordinatively unsaturated Fe^{3+} based activatable probes for enhanced MRI and therapy of tumors, Angew. Chem. Int. Ed. 58 (32) (2019) 11088–11096.

[35] F. Liu, X. He, H. Chen, J. Zhang, H. Zhang, Z. Wang, Gram-scale synthesis of coordination polymer nanodots with renal clearance properties for cancer theranostic applications, Nat. Commun. 6 (2015) 8003.

[36] H. Ejima, J.J. Richardson, K. Liang, J.P. Best, M.P. van Koeverden, G.K. Such, J. Cui, F. Caruso, One-step assembly of coordination complexes for versatile film and particle engineering, Science 341 (6142) (2013) 154–157.

[37] C. Pan, M. Ou, Q. Cheng, Y. Zhou, Y. Yu, Z. Li, F. Zhang, D. Xia, L. Mei, X. Ji, Z-Scheme heterojunction functionalized pyrite nanosheets for modulating tumor microenvironment and strengthening photo/chemodynamic therapeutic effects, Adv. Funct. Mater. 30 (2019) 1906466.

[38] A. Seiler, M. Schneider, H. Förster, S. Roth, E.K. Wirth, C. Culmsee, N. Plesnila, E. Kremmer, O. Rådmark, W. Wurst, G.W. Bornkamm, U. Schweizer, M. Conrad, Glutathione peroxidase 4 senses and translates oxidative stress into 12/15-lipoxygenase dependent- and AIF-mediated cell death, Cell Metab. 8 (3) (2008) 237–248.

[39] T. Liu, W. Liu, M. Zhang, W. Yu, F. Gao, C. Li, S.-B. Wang, J. Feng, X.-Z. Zhang, Ferrous-supply-regeneration nanoengineering for cancer-cell-specific ferroptosis in combination with imaging-guided photodynamic therapy, ACS Nano 12 (12) (2018) 12181–12192.

[40] S. Dixon, K. Lemberg, M. Lamprecht, R. Skouta, E. Zaitsev, C. Gleason, D. Patel, A. Bauer, A. Cantley, W. Yang, B. Morrison, B. Stockwell, Ferroptosis: an iron-dependent form of nonapoptotic cell death, Cell 149 (2012) 1060–1072.

[41] S. Yue, P. Zhang, M. Qin, L. Zhu, Y. Qiao, Q. Li, Y. Lu, H. Wu, N. Jiang, C. Liu, M. Winnik, Y. Hou, An enzyme-like activity nanoprobe based on Fe(III)-rutin hydrate biomineral for MR imaging and therapy of triple negative breast cancer, Adv. Funct. Mater. 32 (2022) 2202848.

[42] W. Feng, X. Han, R. Wang, X. Gao, P. Hu, W. Yue, Y. Chen, J. Shi, Nanocatalysts-augmented and photothermal-enhanced tumor-specific sequential nanocatalytic therapy in both NIR-I and NIR-II biowindows, Adv. Mater. 31 (2019) 1805919.

[43] Z. Zeng, C. Zhang, S. He, J. Li, K. Pu, Activatable cancer sono-immunotherapy using semiconducting polymer nanobodies, Adv. Mater. 34 (2022) 2203246.

[44] X. Duan, C. Chan, W. Lin, Nanoparticle-mediated immunogenic cell death enables and potentiates cancer immunotherapy, Angew. Chem. Int. Ed. 58 (3) (2019) 670–680.

[45] Y. Liu, W. Zhen, Y. Wang, S. Song, H. Zhang, $Na_2S_2O_8$ nanoparticles trigger antitumor immunotherapy through reactive oxygen species storm and surge of tumor osmolarity, J. Am. Chem. Soc. 142 (52) (2020) 21751–21757.

[46] M. Wang, M. Chang, P. Zheng, Q. Sun, G. Wang, J. Lin, C. Li, A noble AuPtAg-GOx Nanozyme for synergistic tumor immunotherapy induced by starvation therapy-augmented mild photothermal therapy, Adv. Sci. 9 (2022) 2202332.

[47] Z. Zhou, H. Wu, R. Yang, A. Xu, Q. Zhang, J. Dong, C. Qian, M. Sun, GSH depletion liposome adjuvant for augmenting the photothermal immunotherapy of breast cancer, Sci. Adv. 6 (2020) eabc4373.

[48] Y. Yuan, Z. Feng, S. Li, Z. Huang, Y. Wan, C. Cao, S. Lin, L. Wu, J. Zhou, L. Liao, J. Qian, C. Lee, Molecular programming of NIR-IIb-emissive semiconducting small molecules for in vivo high-contrast bioimaging beyond 1500 nm, Adv. Mater. 34 (2022) 2201263.

[49] H. Yang, H. Huang, X. Ma, Y. Zhang, X. Yang, M. Yu, Z. Sun, C. Li, F. Wu, Q. Wang, Au-doped Ag_2Te quantum dots with bright NIR-IIb fluorescence for in situ monitoring of angiogenesis and arteriogenesis in a hindlimb ischemic model, Adv. Mater. 33 (2021) 2103953.

[50] J. Li, X. Yu, Y. Jiang, S. He, Y. Zhang, Y. Luo, K. Pu, Second near-infrared photothermal semiconducting polymer nanoadjuvant for enhanced cancer immunotherapy, Adv. Mater. 33 (2021) 2003458.